Single ferroelectric phase transition in tris-sarcosine calcium chloride

Veronica Goian,[1] Fedir Borodavka,[1] Dalibor Repček,[1,2] Maxim Savinov,[1] Martin Míšek,[3] Jiří Kaštil,[3] Volodymyr Skoromets,[1] Petr Ondrejkovič,[1] Jan Petzelt,[1] Jiří Hlinka,[1] Petr Kužel,[1] and Stanislav Kamba[1,*]

[1]*Institute of Physics, The Czech Academy of Sciences, Na Slovance 2, 182 00, Prague 8, Czech Republic*

[2]*Faculty of Nuclear Sciences and Physical Engineering, Czech Technical University in Prague, Břehová 7, 115 19 Prague 1, Czech Republic*

[3]*Institute of Physics, The Czech Academy of Sciences, Cukrovarnická 10/112, 160 00 Prague 6, Czech Republic*

(Received 23 September 2023; revised 6 November 2023; accepted 13 November 2023; published 1 December 2023)

To solve the long-standing controversy over the number of ferroelectric phase transitions in $(CH_3NHCH_2COOH)_3CaCl_2$, we performed a comprehensive series of new dielectric, second-harmonic generation (SHG), calorimetric, infrared, and Raman measurements down to 10 K. Detailed analysis of the data excludes other ferroelectric transitions than the one at $T_C = 130$ K from the *Pnma* to $Pn2_1a$ orthorhombic space groups. The observed pseudoproper ferroelectric (possibly ferrielectric) phase transition is driven by a terahertz soft mode in the $E \| b$ spectra, which couples to a critical microwave relaxation (central mode). Below T_C, additional phonons are activated in the infrared and Raman spectra due to the change of selection rules, but all the observed modes can be assigned to orthorhombic $Pn2_1a$ structure without further reduction of the crystal symmetry. We found a weak and strongly frequency-dependent dielectric anomaly in the radiofrequency permittivity $\varepsilon_b'(T)$ close to 65 K, where the second phase transition was previously suggested. This behavior is assigned to the domain wall dynamics. Temperature dependences of the spontaneous polarization, heat capacity, and SHG signal show no indication of any further phase transition below T_C.

DOI: 10.1103/PhysRevB.108.224101

I. INTRODUCTION

Tris-sarcosine calcium chloride $(CH_3NHCH_2COOH)_3CaCl_2$ (TSCC) is a weak ferroelectric that became known in the 1960s [1]. It undergoes a second-order ferroelectric (FE) phase transition (PT) at $T_C = 130$ K from the orthorhombic space group $D_{2h}^{16} - Pnma$ $(Z = 4)$ to another orthorhombic structure $C_{2v}^{9} - Pn2_1a$ $(Z = 4)$, manifested by a weak Curie-Weiss dielectric anomaly with a very small Curie constant C ($C \approx 5$ K [1] or $C \approx 40$ K in better crystals [2]). Such a behavior is characteristic of so-called pseudoproper ferroelectrics [3,4], termed later independently as weak ferroelectrics [5], where the order parameter is weakly linearly coupled to the polarization [3]. These materials undergo ferrodistortive (equitranslational) PT without multiplication of the primitive unit-cell volume, unlike improper ferroelectrics, where the order parameter is quadratically coupled to the polarization, and a multiplication of the unit cell usually occurs [3]. In TSCC, the order parameter of the pseudoproper ferroelectric phase is a structural change connected with a weak dipole moment only. The typical feature of such a phase is that it deviates only slightly from another higher-symmetry nonpolar structure [5]. For TSCC, such a structure actually exists as a hexagonal superstructure (hypothetical prototypic phase) [6], which frequently causes splitting of the actual room-temperature crystal structure into three types of ferroelastic domains, which mix the a and c axes. Since these ferroelastic domains, which might exist from the crystal growth at high temperatures, would complicate the interpretation of the low-temperature experiments, it is necessary to check their absence at room temperature in a polarizing microscope before all experiments, or to remove them by appropriate mechanical stress.

Recently, using the idea of nonzero dipole moments of the four TSCC molecules (mainly due to the sarcosine) in the unit cell, Scott *et al.* [7] suggested that from a structural point of view, the PT in TSCC can be classified as ferrielectric, since the unit-cell polarization consists of four TSCC molecule dipole moments, which compensate each other in the paraelectric phase but do not cancel in the FE (or ferrielectric [7]) phase.

Concerning the dynamic origin, the PT in TSCC is predominantly of displacive type since a clear underdamped paraelectric soft phonon was observed in the terahertz (THz) spectra [8], as well as in the FE phase by infrared (IR) [9] and Raman spectroscopy [9–14] (the soft mode is not Raman-active in the paraelectric phase). The soft phonon mode is accompanied by a critical relaxational central mode with the main dispersion in the GHz range observed several times in the high-frequency dielectric spectra [15–20], as well as in Brillouin light scattering spectra [21–23], and it was shown to be coupled with the soft phonon [18,24]. The most recent paper by Mackeviciute *et al.* [20] reports an ideal softening of a single soft phonon mode excitation from THz spectra down to 1 GHz. However, these conclusions were erroneous, since they compare in their Fig. 3 the soft mode frequency data taken from [8] in linear-frequency units with their own microwave data expressed in angular frequency units. Thus,

*Author to whom correspondence should be addressed: kamba@fzu.cz

 ©2023 American Physical Society

the spectra of the soft phonon and the central mode are in fact separated, even if overdamped close to T_C. In Ref. [24] it was shown that the central mode is of an intrinsic nature, but it appears only up to 20 K above T_C, where also nonclassical logarithmic corrections to the static permittivity were previously observed [25,26]. Therefore, TSCC appears to be the first ferroelectric in which the appearance of a central mode provides the proof for dynamic critical behavior close to T_C.

Haga *et al.* [27] reported, on the basis of a weak specific-heat anomaly, another PT in TSCC at $T_{C2} = 65$ K. Subsequently, weak anomalies in birefringence and low-frequency permittivity $\varepsilon'_b(T)$ were observed near the same temperature; however, no anomaly was seen in the spontaneous polarization (P_S) [28]. Also, earlier work of Matsuo *et al.* [29] did not reveal any anomalies near T_{C2} in their specific-heat data. Later on, an anomaly near 65 K was observed also in the ^{1}H NMR linewidth and spin-lattice relaxation time T_1 [30] and in the resonant ultrasonic response [31]. Unfortunately, no complete structural data are available below 65 K. The structure was fully determined by x-ray diffraction only at room temperature [32] and in the FE phase at 118 K [33]. Scott *et al.* [7] published incomplete x-ray and neutron diffraction data below T_C down to 20 K showing a temperature dependence of the Ca-O-C bond angle and Ca-sarcosine distance with anomalies near T_C, but no changes near the expected second PT temperature were observed. The thermal expansion coefficient exhibited a small anomaly near 48 K, which was explained by possible PT due to some rearrangements of hydrogen ions without any symmetry change [7]. The existing low-temperature polarization $P_s(T)$ data [7,28] also do not indicate any temperature anomaly and give no evidence of any symmetry change below 65 K, thus the origin of the suggested PT near T_{C2} remains a puzzle.

To reinvestigate this puzzle, we decided to study some missing low-temperature properties of the TSCC crystal. It appears that the dielectric properties were fully published only for the polarization $E \parallel b$ [1], and an absence of dielectric anomalies and pyroelectric currents for $E \parallel a$ and c was just mentioned without showing the data. Concerning the high-frequency and IR properties, only the soft mode and critical relaxation properties are known for the $E \parallel b$ spectra where, moreover, some disagreement between the IR reflectivity and Raman soft mode data below T_C was observed [9,34,35]. No dielectric, THz, and IR data for $E \parallel a$ and $E \parallel c$ were published, although it might help to distinguish the lower symmetry below T_{C2}. Therefore, we fill this gap to get confidence that the symmetry below T_C does not change anymore and remains orthorhombic. We complemented the above-mentioned measurements by the temperature dependence of P_S from hysteresis loops with measurements of the SHG signal along all three crystal axes and with specific-heat data. Our results clearly confirm the absence of any further PT below T_C down to 10 K.

II. EXPERIMENTAL DETAILS

The TSCC crystals were grown by the evaporation method from an aqueous solution of pure sarcosine and calcium chloride in stoichiometric proportions. Details of the crystal growth were published elsewhere [9]. High-quality crystals with a volume of several cm^3 were colorless and optically transparent. The same crystals were used in prior studies [9,12,36]. Although the crystal is hygroscopic in contact with water, it is very stable in the air. X-ray diffraction confirmed the previously published lattice parameters [1] as well as the orthorhombic crystal structure at room temperature. We have cut and polished the crystal for various measurements and found that washing the sample with alcohol disturbs the surface due to the presence of small amounts of water in the alcohol. Therefore, we always used a fresh surface of the sample that did not meet water or alcohol before the measurements.

Low-temperature IR reflectivity measurements in the frequency range 30–670 cm^{-1} (≈1–20 THz) were performed using a Fourier-transform IR spectrometer Bruker IFS-113v equipped with a liquid-He-cooled Si bolometer (operating at 1.6 K) serving as a detector. Room-temperature mid-IR spectra were obtained up to 5000 cm^{-1} using a pyroelectric deuterated triglycine sulfate detector. The THz complex transmittance from 3 to 100 cm^{-1} was measured using a custom-made time-domain spectrometer utilizing a Ti:sapphire femtosecond oscillator (Coherent, Mira) [37]. Its pulse train generates picosecond THz pulses in an interdigitated photoswitch TeraSED [38]; for phase-sensitive electro-optic detection, we use 1-mm-thick (110) oriented ZnTe crystal [39]. For the low-temperature IR reflectivity and THz transmission, Oxford Instruments Optistat cryostats with polyethylene and mylar windows, respectively, were used.

Polarized Raman measurements were performed using a Renishaw RM1000 Micro-Raman spectrometer equipped with Bragg filters and an Ar$^+$ ion laser operating at 514.5 nm. The measurements were conducted in a backscattering geometry in the 5–4000 cm^{-1} range. The sample was cooled down using an Oxford Instruments Microstat continuous flow optical He cryostat.

The SHG measurements were performed using a setup powered by a Ti:sapphire femtosecond laser amplifier (Spitfire ACE) with output at 800 nm, 40 fs pulse length, and 5 kHz repetition rate. Samples placed in a continuous-flow cryostat were illuminated by a collimated polarized beam with a diameter of 1.5–2.0 mm and fluence of 2.5 mJ/cm^2. After appropriate spectral filtering, the SHG signal at 400 nm generated in transmission configuration was detected by an avalanche photodiode. Schema of the SHG experimental setup is shown in Fig. S1 [40].

Radiofrequency dielectric measurements were performed using a Novocontrol Alpha-AN High Performance Impedance Analyzer in conjunction with a JANIS ST-100 cryostat (5–300 K). The FE hysteresis loops were measured at frequencies of 1–50 Hz and temperatures between 8 and 130 K.

The heat capacity was measured using several methods. First, we used the standard 2-τ relaxation method within a PPMS apparatus (Quantum Design Ltd.). This is a standard technique to measure the specific heat of the sample accurately, however with a limited sensitivity. The sample was polished and cut into a small rectangular piece weighing 0.4 mg. It was then mounted on the sapphire measurement platform using apiezon vacuum grease. A heat pulse was applied, and the temperature response of the sample (temperature rise followed by a relaxation to the base temperature)

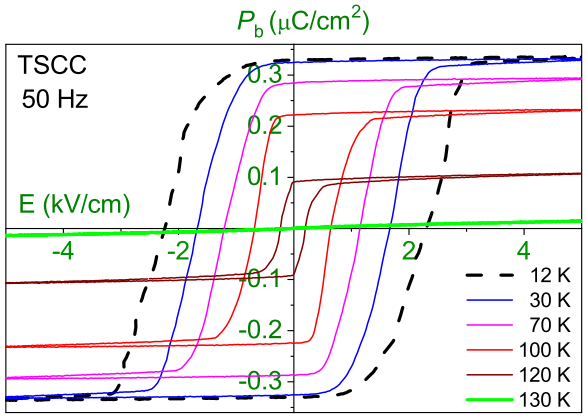

FIG. 1. Ferroelectric hysteresis loop measured from 130 K down to 12 K along the *b* direction.

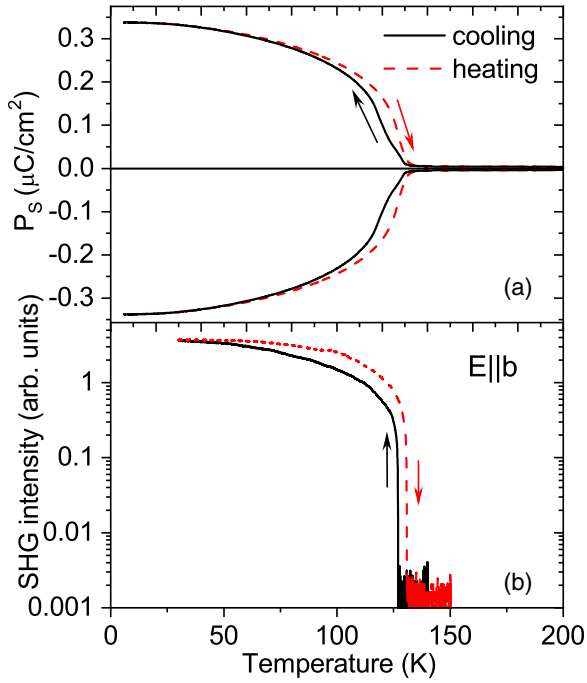

FIG. 2. (a) Temperature dependence of saturated polarization measured along the *b* direction; (b) temperature dependence of the SHG signal measured along the *b* direction. All the measurements were performed on cooling and heating.

was recorded and fitted using a relaxation model. To obtain the heat capacity of the sample, the heat capacity of the empty sapphire platform was subtracted from the measured data. This method is particularly useful when the heat capacity can be assumed to be almost constant within the range of the applied temperature rise. However, it may underestimate the heat capacity in the case of sharp first-order transitions. To elucidate the possible presence of the second (low-temperature) transition, two more heat capacity measurement techniques have been used: (a) "single-slope" analysis within PPMS, and (b) modulation calorimetry [41]. With both of these methods, it is difficult to accurately determine the absolute values of the heat capacity; however, they can provide higher sensitivity of measurement, especially in the case of first-order PTs. For ac modulation heat-capacity measurements, the crystal was thinned down to ≈50 μm to minimize the noise caused by thermal dissipation on the sample. The TSCC crystal was glued to a small heater supplied by a sinusoidal voltage source of a lock-in amplifier. The temperature response of the sample was recorded using a microsized thermocouple (type K) employing the lock-in technique at the second-harmonic frequency. The heat capacity is then inversely proportional to the amplitude of thermal oscillations [41].

III. RESULTS AND DISCUSSION

A. Dielectric permittivity and hysteresis loops

To apply 5 kV/cm for the FE hysteresis loops measurement, the sample was thinned down to 600 μm. FE loops at 50 Hz of well-symmetric shape are shown in Fig. 1. We would like to note that a strongly asymmetric hysteresis loop resembling an antiferroelectric loop was published in Ref. [7]. A similar loop we obtained only when the surface of the hygroscopic TSCC crystal was etched with alcohol containing a small amount of water that disturbs the surface of the sample. The hysteresis loop was measured along the *b* polar axis from 130 K down to 10 K. For $E \parallel a$ and $E \parallel c$, no hysteresis loops were detected down to 10 K. This means that the crystal structure cannot be monoclinic below T_{C2}, which was proposed by Roth *et al.* [36]. Also the temperature dependence of saturated polarization measured along the *b* direction exhibits no anomaly near the T_{C2}. The polarization gradually reduces on heating and disappears above T_C, which is typical for the second-order PTs—see Fig. 2(a). We have also measured the SHG signal in order to check whether any anomaly could be observed close to the expected T_{C2} [see Fig. 2(b)]. The SHG signal starts to rise near $T_C = 130$ K for the laser polarized along the *b* direction, and it shows a gradual increase from T_C down to 40 K without any anomaly near 65 K. We also measured the SHG along the *a* and *c* axes down to 30 K. No signal was detected for those directions, which means that the structure remains orthorhombic with spontaneous polarization only along the *b* axis. Although the FE PT at T_C is of second order, both polarization and SHG show a weak temperature hysteresis due to an imperfect thermal contact.

Complex dielectric permittivity was measured along all three axes between 10 Hz and 1 MHz down to 10 K. The data were taken both on cooling and heating. In Fig. 3(a), the temperature dependences of permittivity at several frequencies are shown. A sharp peak arises near $T_C = 130$ K in ε'_b, and the position of this peak shows a slight temperature hysteresis due to an imperfect thermal contact—see Fig. S2 [40]. The second broader and frequency-dependent peak near 120 K has obviously its origin in increasing FE domain-wall contributions; see Ref. [18]. It shows also a small temperature hysteresis at low frequencies; see Fig. 3(a). This secondary peak was lost when measured in an external bias electric field of 3 kV/cm (see Fig. S2 [40]). The domain-wall motion freezes below 110 K, which leads to the permittivity decrease below this temperature. In the temperature dependence of ε'_a, we have also observed a small anomaly at 130 K which is probably leakage from ε'_b due to a possible small misorientation of the crystal. The behavior of ε'_c at 100 kHz is similar to the case

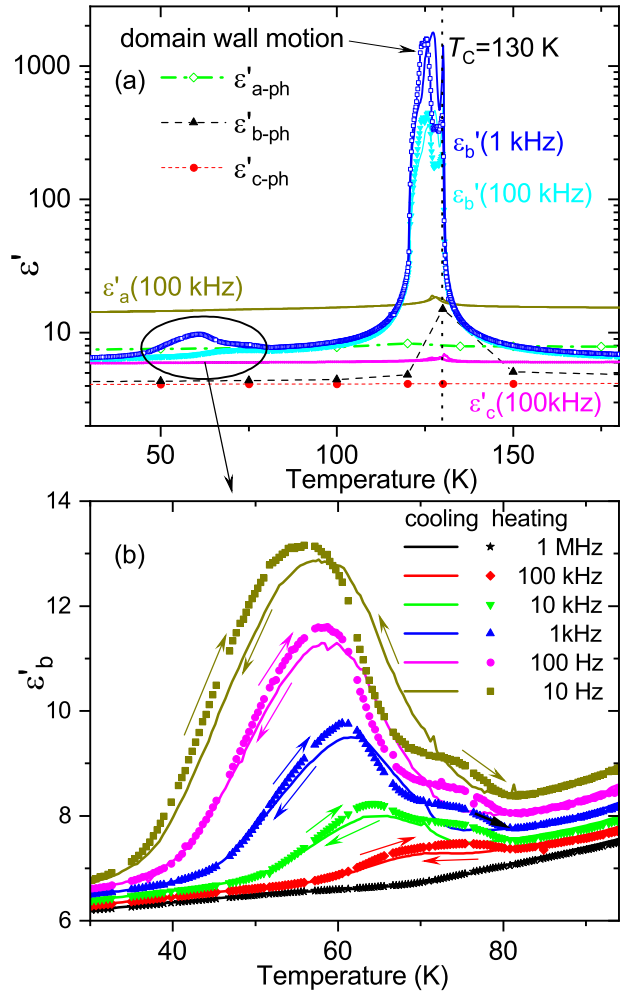

FIG. 3. (a) Temperature dependence of the real part of dielectric permittivity along the a, b, and c directions taken at selected frequencies and low-frequency permittivities $\varepsilon'_{i\text{-ph}}$ ($i = a, b, c$) obtained from fits of THz and IR spectra. The dashed lines are guides for the eyes. Note the logarithmic scale for permittivity. (b) Temperature dependence of ε'_b below 95 K at selected frequencies during cooling (solid lines) and heating (symbols).

of ε'_a, but its value is smaller. Near 60 K, a second broad and frequency-dependent peak is observed in ε'_b [see Fig. 3(b)]. The peak exhibits also a temperature hysteresis. On heating, an additional weak broad peak arises near 75 K. Both peaks are two orders of magnitude smaller than the ε'_b maximum at 120 K, and they weaken with increasing frequencies and vanish at 1 MHz. We assign the peaks to residual domain-wall motion, which completely freezes below 40 K. Since the FE domain structure could be different for cooling and heating, the dielectric response from the domain walls exhibits a weak temperature hysteresis. In Fig. 3(a) we plotted also phonon contributions to the low-frequency permittivities ε'_{a-ph}, ε'_{b-ph}, and ε'_{c-ph} obtained as the static limits from the fits of THz and IR spectra, which, as expected, are slightly smaller than the permittivities at 1 MHz and show no anomaly near 60 K. For more details, see the section about the THz and IR spectra.

To clarify the question of the second PT, we repeated the heat-capacity measurements by Haga *et al.* [27], who reported

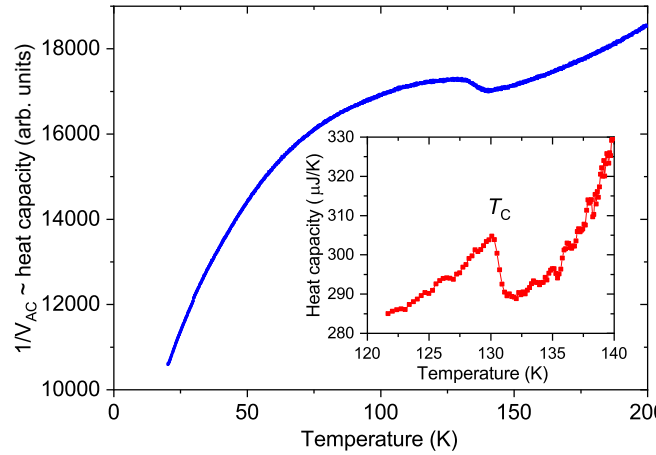

FIG. 4. Temperature dependence of the inverse amplitude of temperature oscillations which are closely related to ac heat capacity. The measurement was performed on 50-μm-thick TSCC crystal. The inset shows the heat capacity of 500-μm-thick sample performed with standard PPMS heat capacity option.

about the weak anomaly near 65 K. In Fig. 4 we plot the temperature dependence of the raw signal of the thermocouple (without any corrections), which is inversely proportional to ac heat capacity. The inset shows the heat capacity obtained using the single-slope technique. One can see clearly the first PT at 130 K, but no other anomalies down to 20 K. Our measurements confirm the earlier work from Matsuo *et al.* [29] where no hint of any second PT was observed. More details about the heat-capacity studies can be found in the Supplemental Material [40].

B. THz permittivity, IR reflectivity, and Raman spectra

Polarized complex THz permittivity spectra are shown in Fig. 5. The ε_b spectra are the most rich. The mode near 55 cm^{-1} is almost temperature-independent, but the lowest-frequency mode (soft mode) softens on cooling towards T_C below our low-frequency limit 5 cm^{-1}. Below T_C the soft mode hardens quickly up to 30 cm^{-1} at 10 K. Intensities of these two phonons decrease on cooling in the FE phase because their oscillator strengths transfer to two additional low-temperature modes near 37 and 45 cm^{-1}. These modes are activated due to the crystal symmetry reduction in the FE phase. The behavior of the soft mode is in agreement with the earlier Refs. [8,24] and confirms the predominantly displacive nature of the FE PT.

THz spectra with polarization $E \parallel a$ and $E \parallel c$ were obtained in a narrower spectral range than the $E \parallel b$ spectra due to a strong phonon absorption above 35 and 40 cm^{-1}, respectively. These phonons are resolved in IR reflectivity spectra (see Fig. 6 and Fig. S3 in [40]). THz values of ε'_a and ε'_c slightly decrease on cooling due to a slight hardening of phonons on cooling caused by the lattice contraction. Below T_C, some new weak modes appear in the ε''_c spectra leaking presumably from the b direction, because their frequencies match each other. Note that although the polar axis is oriented along the b axis, ε'_a has the highest value (see Fig. 5). This is due to two strong polar phonons near 40 cm^{-1}.

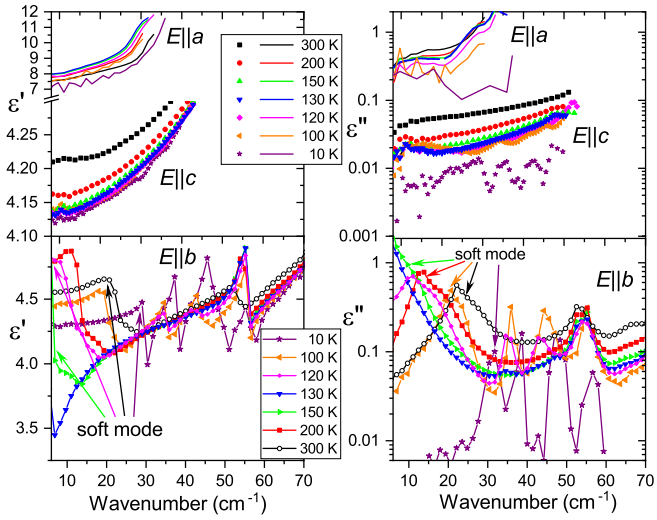

FIG. 5. Components of complex THz permittivity of TSCC measured along all three crystallographic directions below the room temperature. The soft mode absorption in $E \parallel b$ spectra is rather weak, therefore the sample was 2.15 mm thick. The spectra in $E \parallel a$ and $E \parallel c$ were obtained on a 470-μm-thick sample.

Polarized far IR reflectivity spectra are plotted at selected temperatures in Fig. 6. Above 700 cm^{-1}, only the internal sarcosine molecule vibrations contribute to the spectra, which give a small contribution to the permittivity—see the middle IR reflectivity spectra in Fig. S3 [40]. In the far IR range, the phonons correspond to the librations and translations of the sarcosine molecules against the Ca and Cl ions [9]. Below 100 K, the TSCC crystal becomes transparent, and the backside reflectivity plays a significant role in the IR reflectance spectra below 50 cm^{-1}. Therefore, we calculated the reflectivity from the complex THz permittivity, and we display it together with the IR reflectivity spectra in Fig. 6. It can be seen that the reflection band from the soft mode is very weak and therefore difficult to resolve in Fig. 6. This demonstrates the much greater sensitivity of our THz transmission spectra (Fig. 5) to the weak phonon modes than the IR reflectivity. This also explains why the soft mode is barely distinguishable in earlier IR reflectivity spectra [9,12,35], while it was much more accurately determined from the submillimeter transmission spectra [8]. In $E \parallel b$ polarized spectra, three new modes activate near 90, 70, and 50 cm^{-1} below 110 cm^{-1} in the FE phase. Above 100 cm^{-1}, several modes exhibit anomalies near T_C accompanied by the activation of new phonons—see Fig. 7.

The IR reflectivity spectra were fitted using the sum of Lorentz-damped oscillators describing the complex permittivity

$$\varepsilon(\omega) = \varepsilon'(\omega) - i\varepsilon''(\omega) = \varepsilon_\infty + \sum_{j=1}^{n} \frac{\Delta\varepsilon_j \omega_j^2}{\omega_j^2 - \omega^2 + i\omega\gamma_j}, \quad (1)$$

where ω_j, γ_j, and $\Delta\varepsilon_j$ denote the eigenfrequency, damping, and dielectric strength of the jth transverse optical (TO) polar phonon, and ε_∞ marks high-frequency permittivity from electronic transitions. The normal IR reflectivity coefficient $R(\omega)$

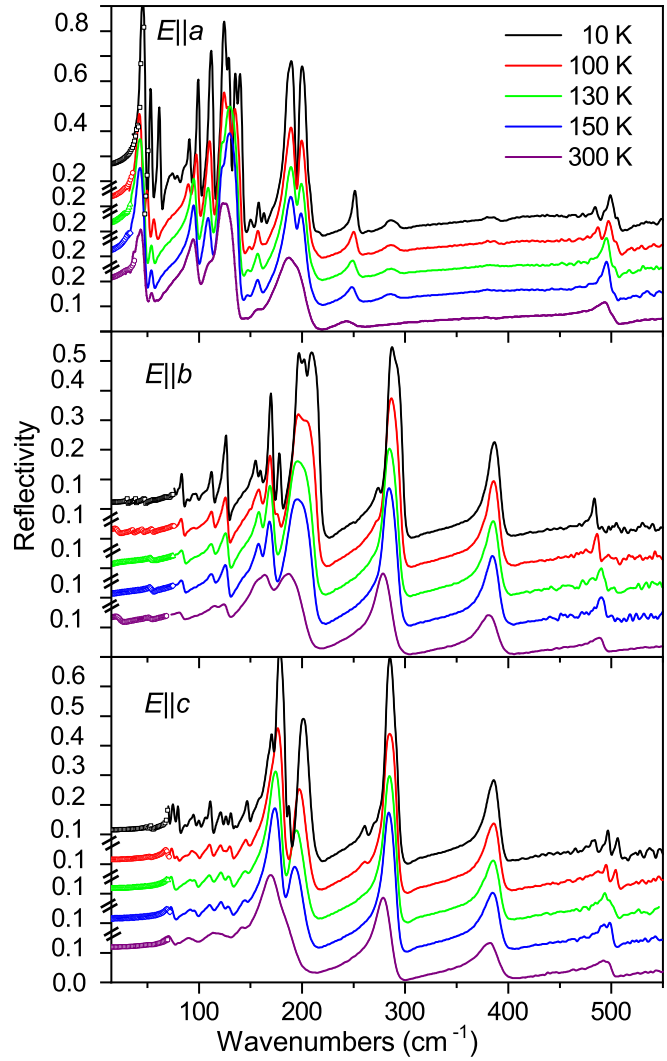

FIG. 6. Polarized IR reflectivity spectra (solid lines) together with THz reflectivity spectra (open symbols) calculated from THz complex permittivity taken at selected temperatures.

is related to the complex permittivity $\varepsilon(\omega)$ by

$$R(\omega) = \left| \frac{\sqrt{\varepsilon(\omega)} - 1}{\sqrt{\varepsilon(\omega)} + 1} \right|^2. \quad (2)$$

In Fig. 7 we show the temperature dependence of polar transverse optical phonon frequencies obtained from the fits. Below T_C, many new phonons start to activate due to the change of crystal symmetry. According to factor group analysis in the FE phase (see [9]), 125 IR-active modes should be active in each polarized IR spectrum as the complete analysis of vibrational modes (including three acoustic modes) yields

$$\Gamma_{Pn2_1a} = 126A_1(b, a^2, b^2, c^2) + 126A_2(ac) + 126B_1(c, bc) + 126B_2(a, ab). \quad (3)$$

One can see that each mode of A_1, B_1, and B_2 symmetry is simultaneously IR- and Raman-active, and $126A_2$ symmetry modes are only Raman-active.

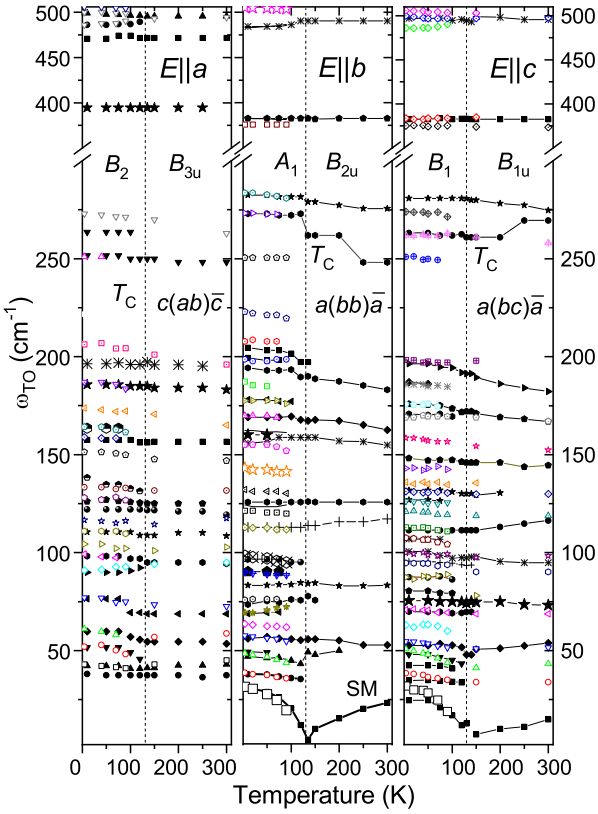

FIG. 7. Temperature dependence of the phonon frequencies in TSCC. Solid and open symbols mark phonons from IR and Raman spectra, respectively. One can see overlapping of some IR and Raman modes in the FE phase, because they have the same symmetries. An optical soft mode (SM) should be seen only in the $E \parallel b$ polarized THz spectra, but its leakage is seen also in the $E \parallel c$ spectra due to small sample misorientation. Many modes activate below T_C due to lowering of the crystal symmetry. Mode symmetries displayed above T_C are valid only for the IR-active modes and below T_C for both IR- and Raman-active modes.

In the paraelectric phase, the factor group analysis of lattice vibrations provides

$$\begin{aligned}\Gamma_{Pnma} = {} & 67B_{1u}(c) + 59B_{2u}(b) + 67B_{3u}(a) \\ & + 67A_g(a^2, b^2, c^2) + 67B_{2g}(ac) + 59A_u(-) \\ & + 59B_{3g}(bc) + 59B_{1g}(ab). \end{aligned} \quad (4)$$

It means that (after the subtraction of an acoustic mode), $58B_{2u}$ symmetry modes are expected in the $E \parallel b$ polarized IR spectra. In the $E \parallel a$ and $E \parallel c$ spectra, 66 optical modes of B_{3u} and B_{1u} symmetry are permitted, respectively [9]. We do not see all of them because only relatively strong modes are discernible in the IR reflectivity spectra (Fig. 6). Also many modes can overlap due to their damping and close frequencies. However, if the FE phase transforms into a monoclinic phase below T_{C2}, the same phonons must, depending on the direction of the FE polarization, activate under T_{C2} in two spectra of different polarization. For example, if the monoclinic structure belongs to a C_2 point group, the original B_1 and B_2 modes from the FE C_{2v} phase will have the same B symmetry, which will be simultaneously active in the $E \parallel a$, $E \parallel c$ polarized IR spectra, and in the bc, ab Raman spectra. However, we do not observe it (except for the weak leakage modes already seen above T_C due to weak sample misorientation).

In the $E \parallel a$ and $E \parallel c$ polarized spectra, the temperature changes in phonon behavior are negligible. Some modes activate only below 100 K, but they are connected with the FE PT at 130 K. In $E \parallel a$ spectra, the phonon modes with the frequencies 42, 52, 60, 76, and 484 cm^{-1} have constant frequencies below 70 K. The situation is different in $E \parallel c$ polarized spectra, where the main phonon anomalies are seen only near T_C. In addition to the soft mode penetrating the $E \parallel c$ polarized spectra from the $E \parallel b$ spectra, we see the activation of three new phonons below 50 cm^{-1} and other modes activate at higher frequencies. Some do activate further away from T_C, but this is due to their weak strength, which increases with cooling, so that they are only resolved in the spectra at lower temperatures.

Low-frequency permittivity $\varepsilon'_{i\text{-ph}}$ $(i = a, b, c)$ defined by the sum of electronic (ε_∞) and phonon contributions $\Delta\varepsilon_j$ can be calculated from the equation

$$\varepsilon'_{i\text{-ph}} = \varepsilon_\infty + \sum_{j=1}^{n} \Delta\varepsilon_j. \quad (5)$$

The resulting permittivities along all the crystallographic axes are plotted in Fig. 3(a) together with the dielectric permittivity in the MHz and kHz range. One can see that the phonon permittivities $\varepsilon'_{a\text{-ph}}$ and $\varepsilon'_{c\text{-ph}}$ do not change with temperature. The anomaly in $\varepsilon'_{b\text{-ph}}$ is much smaller than in the radiofrequency permittivity due to the prevailing contribution of the central mode and domain-wall motion. For a detailed explanation of the lower-frequency dispersion, see the high-frequency and microwave dielectric studies in Refs. [15–20].

Raman spectra can give additional important information about the change in symmetry below the suggested second PT, where the selection rules according to Eq. (3) would not be valid. Therefore, we measured polarized Raman spectra from 300 K down to 4 K in the backscattering geometry along all three crystallographic axes in parallel polarization configurations $a(bb)\bar{a}$, $a(cc)\bar{a}$, and $b(aa)\bar{b}$ (see Figs. 8, S5, and S6) and crossed polarization configurations $c(ab)\bar{c}$ and $a(cb)\bar{a}$ (Figs. S7 and S8). Frequencies of IR- and Raman-active modes and their temperature dependences are compared in Fig. 7.

No additional phonons are observed in Raman spectra below 70 K (see Figs. S5– S8) unlike in previous reports [7,36]. The phonon frequencies in Raman spectra $a(bb)\bar{a}$ and $c(ab)\bar{c}$ are in agreement with previous publication by Chen *et al.* [9]. Activation of the new phonons appears only in the $a(bb)\bar{a}$, $c(ab)\bar{c}$, and $a(cb)\bar{a}$ spectra below 130 K and it is related to the FE PT. Activation of the IR-active soft mode in the Raman spectra below T_C and its pronounced hardening on cooling are also very well seen, in agreement with the THz spectra (see Figs. 8, S5, and S6 [40]).

IV. CONCLUSIONS

We have presented a detailed study of the complex dielectric spectra along all three crystallographic axes of the TSCC crystal in a broad frequency range from several Hz

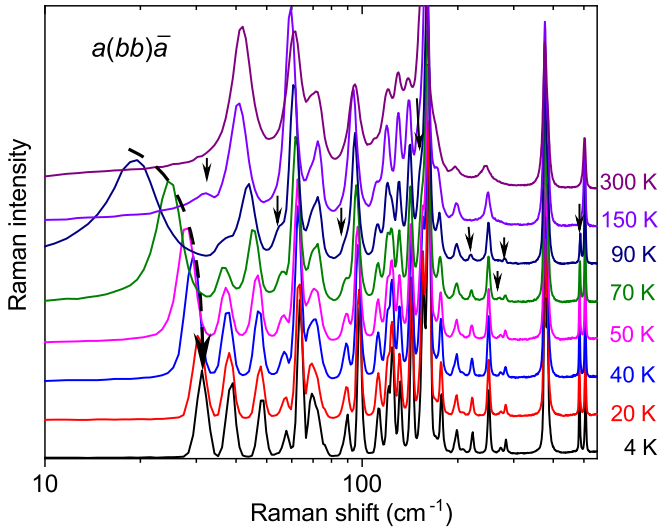

FIG. 8. Temperature dependence of polarized Raman spectra of the TSCC crystal in the $a(bb)\bar{a}$ scattering geometry. Activation of the soft mode below T_C and its hardening is clearly seen on cooling. Other newly activated phonons in the FE phase are marked by black arrows.

up to 20 THz. ε_b' exhibits a sharp peak at $T_C = 130$ K due to the pseudoproper FE PT and two additional frequency-dependent peaks near 120 and 60 K due to domain-wall dynamics. No hints of any phase transition were seen below T_C in the temperature dependence of specific heat, spontaneous polarization, and in the SHG signal. A broad and strongly frequency-dependent peak was observed in the radiofrequency ε_b' spectra, but since it vanishes for frequencies above the MHz range, it was assigned to the domain-wall dynamics. In the IR and Raman polarized spectra, no evidence of another phase transition was seen. Several new modes activate below the FE PT, which was explained within the ferroelectric $Pn21a$ structure. In conclusion, our data do not confirm earlier studies suggesting a second phase transition in the vicinity of 65 K. The second phase transition observed by some authors may be due to an inferior quality of the samples or to a degradation of their surface during grinding and polishing of the hygroscopic TSCC crystal.

ACKNOWLEDGMENTS

We thank Prof. G. Schaack for providing us with high-quality single crystals, and P. Béreš for technical assistance during Raman measurements. The research was supported by the Czech Science Foundation (Project No. 21-06802S) and Grant Agency of the Czech Technical University in Prague (Project No. SGS22/182/OHK4/3T/14). Some experiments were performed in MGML [42], which is supported within the program of Czech Research Infrastructures (Project No. LM2023065).

[1] Y. Makita, J. Phys. Soc. Jpn. **20**, 2073 (1965).
[2] J. Bornarel and H. V. Schmidt, J. Phys. C **14**, 2017 (1981).
[3] V. Dvořák, Ferroelectrics **7**, 1 (1974).
[4] J. Petzelt, J. Grigas, and I. Mayerova, Ferroelectrics **6**, 225 (1973).
[5] K. A. Tagantsev, Ferroelectrics **79**, 57 (1988).
[6] A. Sawada, M. Yasuharu, and Y. Takagi, J. Phys. Soc. Jpn. **42**, 1918 (1977).
[7] J. F. Scott, F. D. Morrison, A. M. Z. Slawin, P. Lightfoot, R. Clulow, A. S. A. Gherson, A. M. Bumstead, J. Gardner, S. C. Capelli, M. R. Probert, S. Sahoo, J. S. Young, R. S. Katiyar, and E. K. H. Salje, Phys. Rev. B **95**, 094119 (2017).
[8] G. V. Kozlov, A. A. Volkov, J. F. Scott, G. E. Feldkamp, and J. Petzelt, Phys. Rev. B **28**, 255 (1983).
[9] T. Chen and G. Schaack, J. Phys. C **17**, 3801 (1984).
[10] S. D. Prokhorova, G. A. Smolensky, I. G. Siny, E. G. Kuzminov, V. D. Mikvabia, and H. Arndt, Ferroelectrics **25**, 629 (1980).
[11] G. E. Feldkamp, J. F. Scott, and W. Windsch, Ferroelectrics **39**, 1163 (1981).
[12] T. Chen, G. Schaack, and V. Winterfeldt, Ferroelectrics **39**, 1131 (1981).
[13] M. Sugo, M. Kasahara, M. Tokunaga, and I. Tatsuzaki, J. Phys. Soc. Jpn. **53**, 3234 (1984).
[14] V. I. Torgashev, Y. I. Yuzyuk, G. Y. Shitov, and P. N. Timonin, Phys. Rev. B **46**, 3657 (1992).
[15] K. Deguchi, N. Aramaki, E. Nakamura, and K. Tanaka, J. Phys. Soc. Jpn. **52**, 1897 (1983).
[16] A. Sawada and M. Horioka, Jpn. J. Appl. Phys. **24**, 390 (1985).
[17] E. Nakamura, K. Itoh, K. Deguchi, and N. Mishima, Jpn. J. Appl. Phys. **24**, 393 (1985).
[18] C. Z. Pawlaczyk, H.-G. Unruh, and J. Petzelt, Phys. Status Solidi B **136**, 435 (1986).
[19] M. Fujimoto, K. Itoh, C. Z. Pawlaczyk, and H.-G. Unruh, Philos. Mag. B **60**, 919 (1989).
[20] R. Mackeviciute, M. Ivanov, J. Banys, N. Novak, Z. Kutnjak, M. Wencka, and J. F. Scott, J. Phys.: Condens. Matter **25**, 212201 (2013).
[21] T. Hikita, P. Schnackenberg, and H. Schmidt, Ferroelectrics **63**, 107 (1985).
[22] J. T. Wang and V. H. Schmidt, Phys. Rev. B **34**, 416 (1986).
[23] L.-T. Cheng and K. A. Nelson, Phys. Rev. B **39**, 9437 (1989).
[24] J. Petzelt, A. A. Volkov, M. A. Goncharov, J. Albers, and A. Klöpperpieper, Solid State Commun. **73**, 5 (1990).
[25] E. Sandvold and E. Courtens, Phys. Rev. B **27**, 5660 (1983).
[26] P. Vaněk, A. Klöpperpieper, and J. Albers, Ferroelectrics **106**, 333 (1990).
[27] H. Haga, A. Onodera, H. Yamashita, and Y. Shiozaki, J. Phys. Soc. Jpn. **62**, 1857 (1993).
[28] H. Haga, A. Onodera, H. Yamashita, and Y. Shiozaki, Ferroelectrics **159**, 55 (1994).
[29] T. Matsuo, M. Mansson, and S. Sunner, Acta Chem. Scand. A **33**, 781 (1979).
[30] K. Lee, M. Lee, S. L. Kwang, and A. R. Lim, J. Phys. Chem. Solids **66**, 1739 (2005).

[31] S. P. P. Jones, D. M. Evans, M. A. Carpenter, S. A. T. Redfern, J. F. Scott, U. Straube, and V. H. Schmidt, Phys. Rev. B **83**, 094102 (2011).
[32] T. Ashida, S. Bando, and M. Kakudo, Acta Cryst. B **28**, 1560 (1972).
[33] N. Mishima, K. Itoh, and E. Nakamura, Acta Cryst. C **40**, 1824 (1984).
[34] T. Chen and G. Schaack, J. Phys. C **17**, 3821 (1984).
[35] M. Iwata, M. Hayashi, and T. Yamamoto, Ferroelectr. Lett. Sect. **19**, 131 (1995).
[36] R. Roth, G. Schaack, and H. D. Hochheimer, Solid State Commun. **55**, 121 (1985).
[37] P. Kužel, H. Němec, F. Kadlec, and C. Kadlec, Opt. Express **18**, 15338 (2010).
[38] A. Dreyhaupt, S. Winnerl, T. Dekorsy, and M. Helm, Appl. Phys. Lett. **86**, 121114 (2005).
[39] Q. Wu, M. Litz, and X.-C. Zhang, Appl. Phys. Lett. **68**, 2924 (1996).
[40] See Supplemental Material at http://link.aps.org/supplemental/10.1103/PhysRevB.108.224101 for additional THz, IR, and Raman spectra together with a detailed description of SHG and heat capacity measurements.
[41] Y. Kraftmakher, *Modulation Calorimetry I* (Springer Berlin, Heidelberg, 2004).
[42] mgml.eu.